CMS Physics Analysis Summary

Contact: cms-pag-conveners-higgs@cern.ch 2018/01/30

Search for Higgs bosons produced in association with b quarks and decaying into a b-quark pair with 13 TeV data

The CMS Collaboration

Abstract

A search for Higgs bosons that decay into a b quark-antiquark pair and are accompanied by at least one additional b quark is performed with the CMS detector. The data analyzed were recorded in proton-proton collisions at a centre-of-mass energy of 13 TeV at the LHC, corresponding to an integrated luminosity of 35.7 fb^{-1}. The final state considered is particularly sensitive to signatures of a Higgs sector beyond the standard model, as predicted by the minimal supersymmetric standard model (MSSM) and the two Higgs doublet model (2HDM) with large values of the parameter $\tan\beta$. No signal above the standard model background expectation is observed. Stringent upper limits on the cross section times branching fraction are set for Higgs bosons with masses up to 1300 GeV at 95% confidence level. The results are interpreted within several MSSM and 2HDM scenarios. In the hMSSM scenario, upper limits on $\tan\beta$ are obtained, ranging from 22 to 60 for Higgs masses from 300 to 900 GeV. In the flipped 2HDM scenario, similar upper limits on $\tan\beta$ are set over the full $\cos(\beta-\alpha)$ range and for Higgs masses from 300 to 850 GeV.

1 Introduction

A light standard model (SM) Higgs boson has a large coupling to b quarks via Yukawa interaction. Its production in association with b quarks and subsequent decay into b quarks at the CERN LHC is, however, buried by the high rate of heavy-flavour multijet production. There are, nevertheless, models beyond the SM (BSM) that predict an enhancement of Higgs boson production in association with b quarks, which motivate the search for such processes.

Prominent examples of BSM models are the minimal supersymmetric extension of the SM (MSSM) [1] and two Higgs doublet models (2HDM) [2], which contain two scalar Higgs doublets. In the simplest case, these result in two charged Higgs bosons, $H^{\pm}$, and three neutral ones, jointly denoted as ϕ. Among the latter are one CP-odd (A), and two CP-even (h, H) states, where h denotes usually the lighter CP-even state. For the purpose of this analysis, the boson discovered in 2012 with a mass near 125 GeV [3–5] is interpreted as h, whose mass is thus constrained to the measured value. The two heavier neutral states, H and A, are subject of the search presented here.

The 2HDM does a priori not conserve CP and may allow flavour-changing neutral currents. In order to suppress such features at tree level, discrete symmetries are imposed, which limit the choice of Higgs doublets that the fermions can couple to. This leads to four types of models with natural flavour conservation at tree level:

- **type-I**: all fermions couple to the same doublet;
- **type-II**: up-type fermions (u, c, t) couple to one, down-type fermions (d, s, b, e, μ, τ) couple to the other doublet. This structure is also implemented in the MSSM;
- **lepton-specific**: all leptons couple to one, all quarks couple to the other doublet;
- **flipped**: leptons and up-type quarks couple to one, down-type quarks to the other doublet.

While until now the type-I and type-II models have been most intensively tested experimentally, the flipped model is remarkably unexplored from the experimental side. The $H/A \to b\bar{b}$ decay mode is ideally suited to constrain this model due to the large branching fraction of the Higgs boson into b quarks.

The CP-conserving 2HDM have seven free parameters. The can be chosen as the Higgs boson masses (m_h, m_H, m_A, $m_{H^{\pm}}$), the mixing angle between the CP-even Higgs bosons (α), the ratio of the vacuum expectation values of the two doublets ($\tan\beta = v_2/v_1$), and the parameter that potentially mixes the two Higgs doublets (m_{12}). For $\cos(\beta-\alpha) \to 0$, the light CP-even Higgs boson (h) obtains properties indistinguishable from the SM Higgs boson with the same mass [2] in all four types of models listed above.

The MSSM has the same Higgs sector structure as the 2HDM of type-II. The additional constraints given by the fermion-boson symmetry fix all mass relations between the Higgs bosons and the angle α at tree level, reducing the number of parameters from seven to only two. These parameters are commonly chosen as the mass of the pseudoscalar Higgs boson, m_A, and $\tan\beta$. After the Higgs boson discovery at the LHC [3–5], MSSM benchmark scenarios have been refined to match the experimental data and to reveal characteristic features of certain regions of the parameter space [6, 7]. Considered in this analysis are the $m_h^{\text{mod+}}$, the hMSSM, the light $\widetilde{\tau}$, and the light $\widetilde{t}$ scenarios.

The $m_h^{\text{mod+}}$ scenario is a modification of the m_h^{max} scenario, which was originally defined to give conservative exclusion bounds on $\tan\beta$ in the LEP Higgs searches [8–10]. It has been

modified such that the mass of the lightest CP-even state, m_{h}, is compatible with the mass of the SM particle within ± 3 GeV [6]. The hMSSM approach [11–13] describes the MSSM Higgs sector in terms of just m_{Z}, m_{A}, and $\tan\beta$, plus the experimental knowledge of m_{h}. It defines a largely model-independent scenario, because the predictions for the properties of the MSSM Higgs bosons do not depend on the details of the SUSY sector [14]. The light $\widetilde{\tau}$ and light $\widetilde{\mathrm{t}}$ scenarios define further common MSSM benchmark scenarios, in which the lightest CP-even Higgs production and decay rates are modified to take into account the Higgs boson discovery, which also changes the couplings of $\mathrm{H/A} \to \mathrm{b\bar{b}}$ [6].

For $\tan\beta$ values larger than one, the couplings of the Higgs fields to b quarks are enhanced both in the flipped and the type-II models, and thus also the MSSM. Furthermore, there is an approximate mass degeneracy between the A and H bosons in the MSSM for the studied range of m_{A}. For the 2HDM scenarios considered in this note such a degeneracy will be imposed. These effects enhance the combined cross section for producing these Higgs bosons in association with b quarks by a factor of up to $2\tan^2\beta$. The decay $\mathrm{H/A} \to \mathrm{b\bar{b}}$ is expected to have a high branching fraction, even at large values of the Higgs boson mass and $|\cos(\beta-\alpha)|$ [15]. Beyond the 2HDM and MSSM interpretations, the $\mathrm{b\bar{b}}$ decay mode is also relevant in the more general context of exotic resonance searches, motivated for example by dark-matter models involving mediator particles with a large couplings to b quarks [16, 17].

The most stringent constraints on the MSSM parameter $\tan\beta$ so far, with exclusion limits in the range 4–60 in the mass interval of 90–1600 GeV, have been obtained in measurements at the LHC in the $\phi \to \tau\tau$ decay mode [18–23]. Preceding limits had been obtained by the LEP [8] and the Tevatron experiments [24–26]. The $\phi \to \mu\mu$ decay mode has been investigated as well [19, 27].

In the $\phi \to \mathrm{b\bar{b}}$ decay mode, searches have initially been performed at LEP [8] and by the CDF and D0 Collaborations [28] at the Tevatron collider. At the LHC, the only analyses in this channel with associated b jets are predecessors of the analysis presented here, performed by the CMS Collaboration using the 7 TeV [29] and 8 TeV [30] data. In absence of any signal, limits on the $\mathrm{pp} \to \mathrm{b}\phi(\to \mathrm{b\bar{b}}) + \mathrm{X}$ cross section have been derived in the 90–900 GeV mass range. The combined 2011–12 data analyses translate into upper bounds on $\tan\beta$ between 14 and 50 in the Higgs boson mass range of 100–500 GeV assuming the $m_{\mathrm{h}}^{\mathrm{mod+}}$ scenario of the MSSM.

The ATLAS Collaboration has performed extensive 2HDM interpretations of measurements in the $\mathrm{A} \to \mathrm{Zh}$, $\mathrm{h} \to \mathrm{b\bar{b}}$, decay mode [31, 32], which also cover the flipped scenario. Therefore, the 2HDM interpretations reported in this note are compared to these ATLAS results.

With the large proton-proton (pp) collision data set of $35.7\,\mathrm{fb}^{-1}$ collected at a centre-of-mass energy of 13 TeV in 2016, we extend the previous CMS searches both in mass range and sensitivity. The analysis focuses on neutral Higgs bosons A and H with masses $m_{\mathrm{A/H}} \geq 300$ GeV that are produced in association with at least one b quark and decay to $\mathrm{b\bar{b}}$ as shown by the diagrams in Fig. 1. The signal signature therefore comprises final states characterized by at least three b-tagged jets, and the dominant background is multijet production. A fourth b-tagged jet is not explicitly required, since its kinematic distributions for the signal extend significantly beyond the available acceptance, and the resulting signal efficiency would be very low. Events are selected by dedicated triggers that identify b jets already during data taking. This helps to significantly suppress the large rate of multijet production at the LHC while maintaining sensitivity to the signal process. The analysis searches for a peak in the invariant mass distribution, $\mathrm{M_{12}}$, of the two b jets with the highest p_{T} values, which are assumed to originate from the Higgs boson decay. The dominant background is the production of heavy-flavour multijet events containing either three b jets, or two b jets plus a third jet originating from either a charm

quark, a light-flavour quark or a gluon, which is misidentified as a b quark jet.

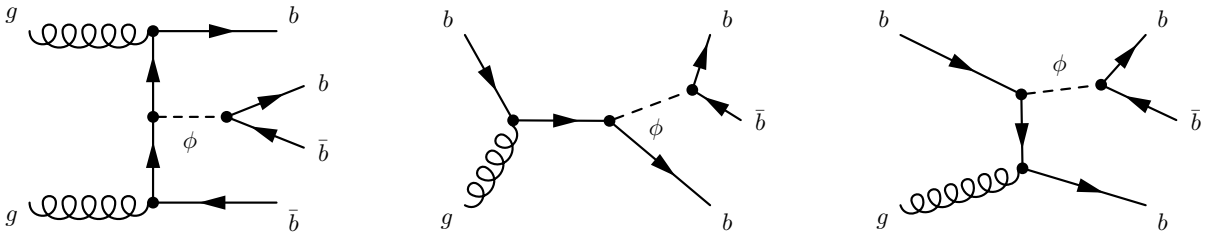

Figure 1: Example Feynman diagrams of the signal processes.

2 The CMS detector

The central feature of the CMS detector is a superconducting solenoid of 6 m internal diameter, providing a magnetic field of 3.8 T. Within the field volume, the inner tracker is formed by a silicon pixel and strip tracker. It measures charged particles within the pseudorapidity range $|\eta| < 2.5$. The tracker provides a transverse impact parameter resolution of approximately 15 μm and a resolution on p_{T} of about 1.5% for 100 GeV particles. Also inside the field volume are a crystal electromagnetic calorimeter, and a brass and scintillator hadron calorimeter. Muons are measured in gas-ionization detectors embedded in the steel flux-return yoke, in the pseudorapidity range $|\eta| < 2.4$, with detector planes made using three technologies: drift tubes, cathode strip chambers, and resistive-plate chambers. Matching muons to tracks measured in the silicon tracker results in a p_{T} resolution between 1% and 5%, for p_{T} values up to 1 TeV. Forward calorimetry extends the coverage provided by the barrel and endcap detectors up to $|\eta| < 5$. A detailed description of the CMS detector, together with a definition of the coordinate system used and the relevant kinematic variables, can be found in Ref. [33].

3 Event reconstruction and simulation

A particle-flow algorithm [34] is used to reconstruct and identify all particles in the event, i.e. electrons, muons, photons, charged hadrons, and neutral hadrons, with an optimal combination of all CMS detector systems.

All events are required to have at least one primary vertex reconstructed within a 24 cm window along the beam axis, with a transverse distance from the nominal pp interaction region of less than 2 cm [35]. The reconstructed vertex with the largest value of summed physics objects p_{T}^2 is taken to be the primary pp interaction vertex. The physics objects are the objects returned by a jet finding algorithm [36, 37] applied to all charged tracks associated with the vertex, plus the corresponding associated missing transverse momentum.

Jets are clustered from the reconstructed particle candidates using the anti-k_{T} algorithm [36] with a distance parameter of $R = 0.4$. Each jet is required to pass dedicated quality criteria to suppress the impact of instrumental noise and misreconstruction. Contributions from additional pp interactions within the same bunch crossing (pileup) affect the jet momentum measurement. To mitigate this effect, charged particles associated with other vertices than the reference primary vertex are discarded in the jet reconstruction [38], and residual contributions (e.g. from neutral particles) are accounted for using a jet-area based correction [39]. Jet energy corrections are derived from simulation, and are confirmed with measurements of the energy balance in dijet and Z/γ+jet events [40].

For the offline identification of b jets, the combined secondary vertex (CSVv2) algorithm [41] is used. This algorithm combines information on track impact parameters and secondary vertices within a jet into an artificial neural network classifier that provides a good separation between b jets and jets of other flavours.

Simulated samples of signal and background events, also referred to as Monte Carlo (MC) samples, were produced using different event generators and include pileup events. The MSSM Higgs signal samples, $pp \to b\bar{b}\phi$+X with $\phi \to b\bar{b}$, were produced at leading order (LO) in the 4-flavour scheme with PYTHIA 8.212 [42]. Comparing this prediction to next-to-leading order (NLO) calculations [43] generated using MADGRAPH5_aMC@NLO in version 2.3.0 [44, 45], we find a very good agreement in the shapes of the leading dijet invariant mass distribution, M_{12}, while the selection efficiency is up to 10% lower when using the NLO prediction. We correct the NLO effect by applying mass dependent scale factors to the LO signals and assign a corresponding systematic uncertainty in the final results. The multijet background from quantum chromodynamics (QCD) processes has been simulated with the MADGRAPH 5 event generator [46, 47]. The NNPDF 3.0 [48] parton distribution functions (PDF) are used in all generated samples. For all generators, fragmentation, hadronization, and the underlying event have been modelled using PYTHIA with tune CUETP8M1 [49]. The response of the CMS detector is modelled with GEANT4 [50].

4 Trigger and event selection

A major challenge to this analysis is posed by the huge hadronic interaction rate at the LHC. It is addressed with a dedicated trigger scheme [51], especially designed to suppress the multijet background. Only events with at least two jets in the pseudorapidity range of $|\eta| \leq 2.4$ are selected. The two leading jets are required to have $p_T > 100\,\text{GeV}$, and the event is only accepted if the absolute value of the difference in pseudorapidity, $\Delta\eta$, between any two jets fulfilling the p_T and η requirements, is less than or equal to 1.6. The tight online requirements on the angular variables of the jets are introduced to reduce the trigger rates while preserving high efficiency in the probed mass range of the Higgs bosons. At the trigger level, b jets are identified using the CSVv2 algorithm with slightly different requirements than for the offline analysis. At least two jets in the event must satisfy the online b tagging criteria.

The efficiency of the jet-p_T requirements in the trigger are derived from data collected with prescaled single-jet triggers with lower threshold. The efficiency in data and simulation is measured as a function of jet p_T and η. The differences between the two are corrected for in the analysis of the simulated samples. The online b tagging efficiencies relative to the offline b tagging selection are obtained from data using prescaled dijet triggers with a single-b-tag requirement. A tag-and-probe method is employed to determine the efficiency as a function of p_T and η of the jets. Efficiencies are found to range from above 80% for $p_T \approx 100\,\text{GeV}$ to around 50% for $p_T \approx 900\,\text{GeV}$, averaged over η.

The offline selection requires at least three jets satisfying $|\eta| \leq 2.2$ and $p_T > 40$ GeV. The first two leading jets should have $p_T > 100$ GeV. The pseudo-rapidity selection is applied to profit from optimal b tagging performance. The three leading jets have to pass the CSVv2 b tag requirement of the medium working point. This working point is chosen such that it features a 1% probability for light-flavour jets (attributed to u, d, s, or g partons) to be misidentified as b jets. The separation between the two leading jets in η has to be less than 1.55, and a minimal pairwise separation of $\Delta R > 1$ between each two of the three leading jets is imposed to suppress background from b quark-antiquark pairs arising from gluon splitting. This sample is referred to as "triple-b-tag" sample in the following.

5 Signal modeling

A signal template is obtained for each MSSM Higgs boson mass considered by applying the full selection to the corresponding simulated signal dataset, for nominal masses in the range of 300–1300 GeV. The sensitivity of this analysis does not extend down to cross sections as low as that of the SM Higgs boson. Thus, a signal model with a single mass peak is sufficient. This is in contrast to the $\phi \to \tau\tau$ analysis [20], where the signal model comprises the three neutral Higgs bosons of the MSSM, one of which is SM-like.

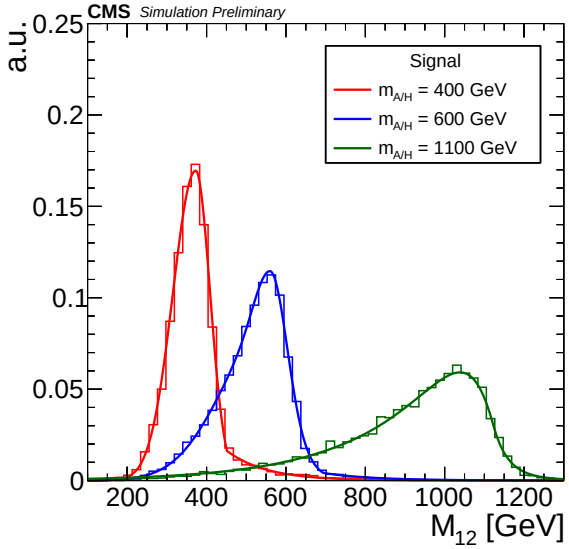

Figure 2: Signal mass distributions and parameterizations as obtained from simulation for different Higgs masses: 400 GeV (red), 600 GeV (blue), and 1100 GeV (green).

The distributions of the invariant mass of the two b jets with the highest p_T values, M_{12}, of the signal templates and parameterizations for different Higgs boson masses are shown in Fig. 2. The natural width expected for a MSSM Higgs boson in the considered mass and $\tan\beta$ region is negligible compared to the detector resolution. At a mass of 500 GeV and $\tan\beta = 60$, for example, the natural width of the mass peak is found to be about 24 GeV in the $m_h^{\text{mod+}}$ scenario, which is only 17% of the full width at half maximum of the reconstructed mass distribution. The shape of the mass distribution is thus dominated by the experimental resolution and wrong-pairing background. The missing momentum from neutrinos in semileptonic decays of hadrons containing bottom and charm quarks results in pronounced tails towards lower masses. The wrong-pairing background gives rise to tails in both directions. For the lower mass points, however, the tails towards lower masses are suppressed because of the p_T thresholds.

The signal efficiency for each Higgs mass point is obtained from simulation and shown in Fig. 3. The efficiency of the kinematic trigger selection has been derived with data from control triggers as described above and is applied as a weight for each event. Scale factors to account for the different b tagging efficiencies in data and MC [41] are also applied. The efficiency ranges between 0.49% and 1.4% and peaks around 500 GeV. The efficiency first increases due to the kinematic selection and then decreases for masses beyond 500 GeV due to the requirement of three b-tagged jets, and the fact that the b tagging efficiency decreases at high jet p_T.

For nominal masses in the lower range of 300–500 GeV, each signal shape is parameterized by two Gaussian functions having the same mean position but different widths on the right-hand and left-hand side of the peak position, continued with an exponential at higher masses to

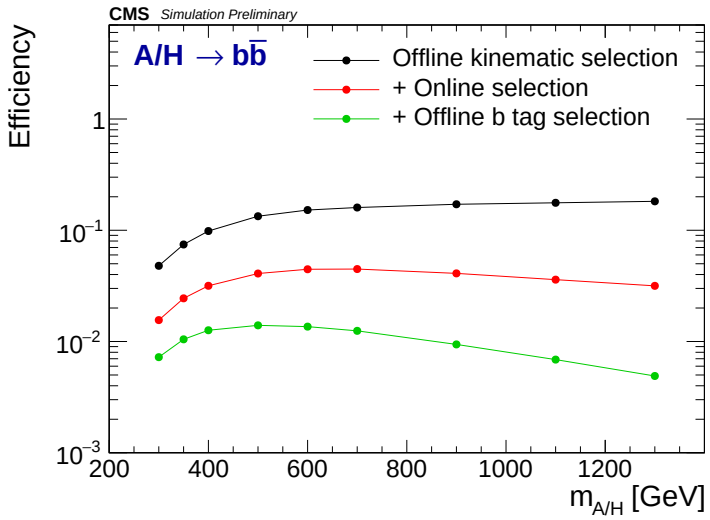

Figure 3: Signal efficiency as a function of the Higgs boson mass after different stages of event selection: offline kinematic selection (black), online trigger selection (red) and offline b tagging selection (green).

describe the observed tail. The function has therefore five parameters. The signal of the 600 GeV mass point requires one additional Gaussian function on each side of the peak position to be able to describe the tails of the distribution. This function thus has nine parameters in total. For nominal masses in the range 700–1300 GeV, a Bukin function, which has again five parameters, is used. All parameterizations give a very good modelling of the M_{12} spectrum.

6 Background model

The main background for this analysis originates from multijet production, with at least two energetic jets actually containing b hadrons, and a third jet that satisfies the b tagging selection but possibly as a result of a mistag. Top quark-antiquark production is found to be negligible and exhibits a shape very similar to the multijet process, it is implicitly included in the data driven estimate.

The relevant features of the multijet background are studied in a suitable control region in the data, which is obtained from the triple-b-tag selection by imposing a b tag veto on the third leading jet. This veto rejects jets that would satisfy a loose b-tag requirement defined by a 10% probability for light-flavour jets to be misidentified as b jets. This "reverse-b-tag" control region has no overlap with the triple-b-tag signal region, while it preserves similar kinematic distributions for the three leading jets. In addition, the signal contamination in the reverse-b-tag control region is negligible. To obtain a similar event statistics as in the signal region, events are randomly dropped from this control sample such that its statistics is reduced by about a factor of 9.

A suitably chosen analytic function is used to model the multijet background. This function is extensively validated in the reverse-b-tag control region. In order to improve the background description and reduce the potential bias related to the choice of the background model, the M_{12} distribution is divided into the three overlapping subranges $[200, 650]$, $[350, 1190]$ and $[500, 1700]$ GeV, whose borders are chosen to cover well the signal shapes of the associated mass points (see Section 5).

In the first subrange, turn-on effects due to kinematic selection play an important role. The chosen function is a product of two terms. The first term is a turn-on function, represented by a Gaussian error function in the form of

$$f(\mathrm{M}_{12}) = 0.5 \cdot \mathrm{Erf}(p_0(\mathrm{M}_{12} - p_1)) + 1), \tag{1}$$

where

$$\mathrm{Erf}(x) = \frac{2}{\sqrt{\pi}} \int_0^x e^{-t^2} dt, \tag{2}$$

and the parameters p_0 and p_1 describe the slope of the turn-on and the turn-on point, respectively.

The falling part of the spectrum is described by an extension of the Novosibirsk function originally used to describe a Compton spectrum [52], defined as:

$$g(\mathrm{M}_{12}) = p_2 \cdot \exp\left(-\frac{1}{2\sigma_0^2}\ln^2[1 - \frac{\mathrm{M}_{12} - p_3}{p_4}p_5 - p_6\frac{(\mathrm{M}_{12} - p_3)^2}{p_4}p_5] - \frac{\sigma_0^2}{2}\right), \tag{3}$$

where p_2 is a normalization parameter, p_3 the peak value of the distribution, and p_4 and p_5 are related to the asymmetry of the spectrum. These parameters are allowed to change between control and signal regions. The variable σ_0 is defined as

$$\sigma_0 = \frac{2}{\xi}\sinh^{-1}(p_5 \cdot \xi/2), \text{ where } \xi = 2\sqrt{\ln 4}. \tag{4}$$

In the second and third subrange, we choose a non-extended Novosibirsk function ($p_6 \equiv 0$) without turn-on factor.

Figure 4 shows the fits of the chosen functions to the control region data. In the first subrange, $\mathrm{M}_{12} = [200, 650]$ GeV, the turn-on effect due to the jet p_T threshold at trigger level is clearly visible. In the other two mass subranges, the spectrum shows only the expected falling behaviour with M_{12}. The values of the parameters p_0 and p_1 used to model the turn-on obtained in the control region are also used for the signal region fit since the turn-on behaviour in the two regions is found to be very similar. The other function parameters are allowed to vary independently in the control and signal region fits.

Different families of other probability density functions (PDFs) such as Bernstein polynomials and the so-called dijet function as defined in Ref. [53] are studied as alternative background models. For each family, a systematic bias on the extraction of a signal with mass $m_{\mathrm{A/H}}$ is determined using toy experiments drawn from a fit with an alternative function to the observed data. Using the nominal Gaussian error plus extended Novosibirsk functions as background model, a maximum-likelihood fit of signal and background is performed for each toy experiment. The extracted and injected numbers of signal events are compared taking into account the statistical uncertainty of the fit. The resulting pull distribution is considered to represent the systematic bias due to the choice of the background function. We observe a bias of 100%, 20%, and 25% for the first, second, and third subrange, respectively.

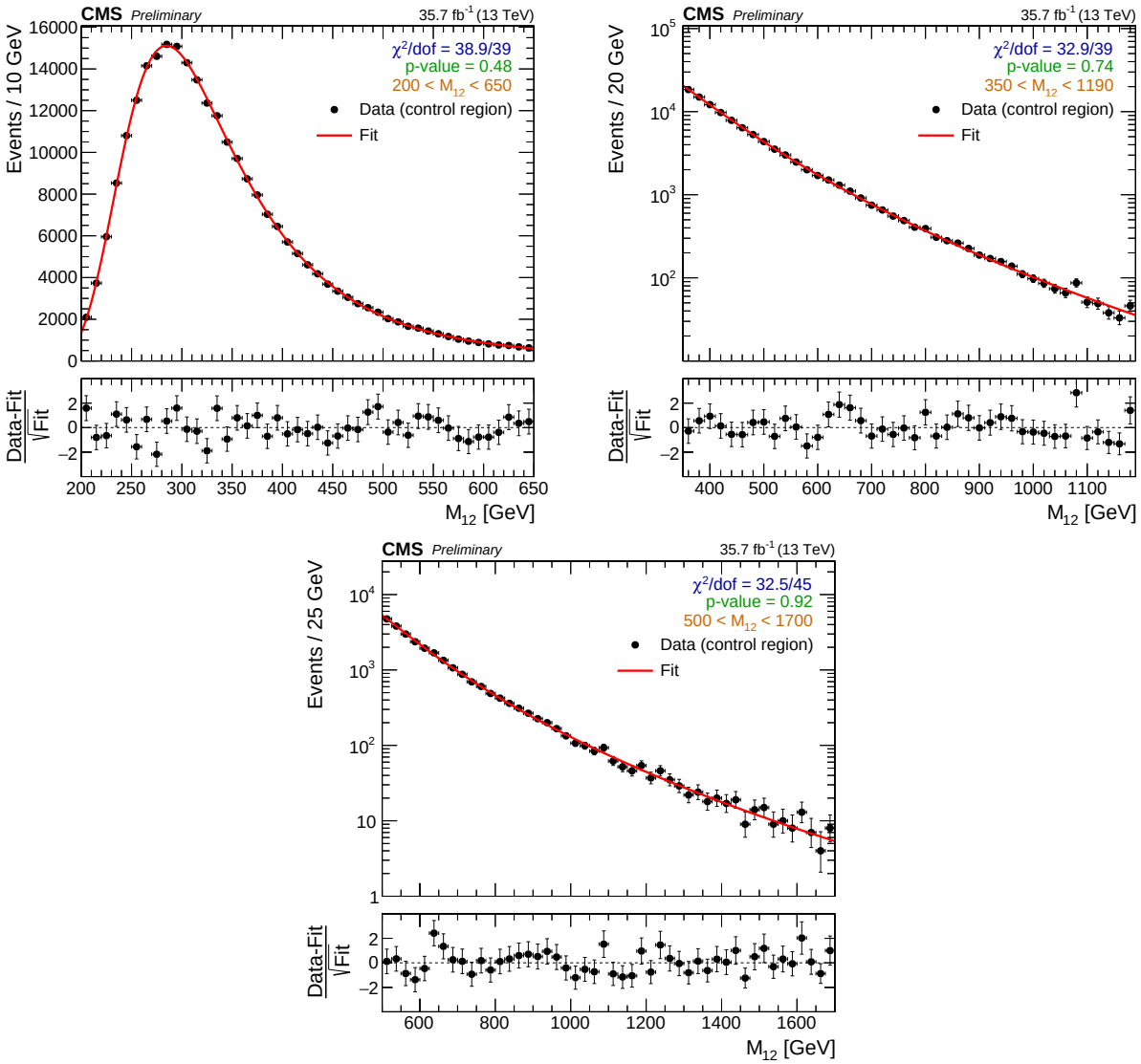

Figure 4: Invariant dijet mass M_{12} in the reverse-b-tag control region in the three subranges used for the fit: $M_{12} = [200, 650]$ GeV (top left) in linear scale, $M_{12} = [350, 1190]$ GeV (top right) and $M_{12} = [500, 1700]$ GeV (bottom) in logarithmic scale. The dots represent the data. The red line is the result of the fit of the background parameterizations described in the text. In the bottom panel of each plot the normalized difference $(\frac{\text{Data}-\text{Fit}}{\sqrt{\text{Fit}}})$ is shown.

7 Systematic uncertainties

The following systematic uncertainties in the expected signal and background estimation affect the determination of the signal yield and/or its interpretation within the MSSM or 2HDM models.

The signal yields are affected by the following uncertainties:

- a 2.5% uncertainty in the estimated integrated luminosity of the data sample [54];
- the uncertainty in the online b tagging efficiency scale factor, which results in an overall uncertainty in the range of 0.8–1.3% for signal masses of 300–1300 GeV;
- a 5% uncertainty in the NLO correction of the selection efficiency.

Uncertainties affecting the shape as well as the normalization of the signal templates are:

- the uncertainty in the jet trigger efficiencies, ranging between 0 and 7% per jet depending on its η and p_{T};
- the uncertainty in the offline b tagging efficiency (2–5% per jet depending on its transverse momentum) and the b-misidentification scale factors ($< 0.3\%$);
- the jet energy scale (JES) and jet energy resolution (JER) uncertainties (1–6%): their impact is estimated by varying the JES and JER in the simulation within the measured uncertainties;
- the effect due to the choice of the PDF following the findings of the LHC Higgs Cross Section Working Group [55];
- the uncertainty in the minimum-bias cross section of 4.6% assumed in the pileup reweighting procedure.

For the background estimation, the bias on the extracted signal as reported in Section 6 is considered as a shape systematic uncertainty. This poses the largest uncertainty for the analysis.

8 Results

The number of potential signal events is extracted by performing a maximum-likelihood fit of the signal plus background parameterizations to the M_{12} data distribution. Initially, a fit with only the background parameterizations is performed. Results of this background-only fit in the three subranges shown in one plot are given in Fig 5. The normalized differences between data and fit together with the post-fit uncertainties are shown for each subrange.

No significant excess over the background-only distribution is observed and upper limits at 95% confidence level (CL) on the cross section times branching fraction
$\sigma(\mathrm{pp} \to \mathrm{bA/H} + \mathrm{X})\,\mathcal{B}(\mathrm{A/H} \to \mathrm{b\bar{b}})$ are derived. The cross section limits are obtained from the fractions determined by the fit multiplied by the total number of data events after the selection in the signal region, and divided by the corresponding signal efficiencies and the integrated luminosity. For the calculation of exclusion limits, the modified frequentist construction $\mathrm{CL_s}$ [56, 57] is adopted using the ROOSTATS package [58]. The chosen test statistic, used to determine how signal- and background-like the data are, is based on the profile likelihood ratio. Systematic uncertainties are treated as nuisance parameters and profiled in the statistical interpretation using log-normal priors, while Gaussian priors are used for shape uncertainties. These uncertainties have been listed in Section 7.

Model-independent upper cross section times branching fraction limits are shown as a function

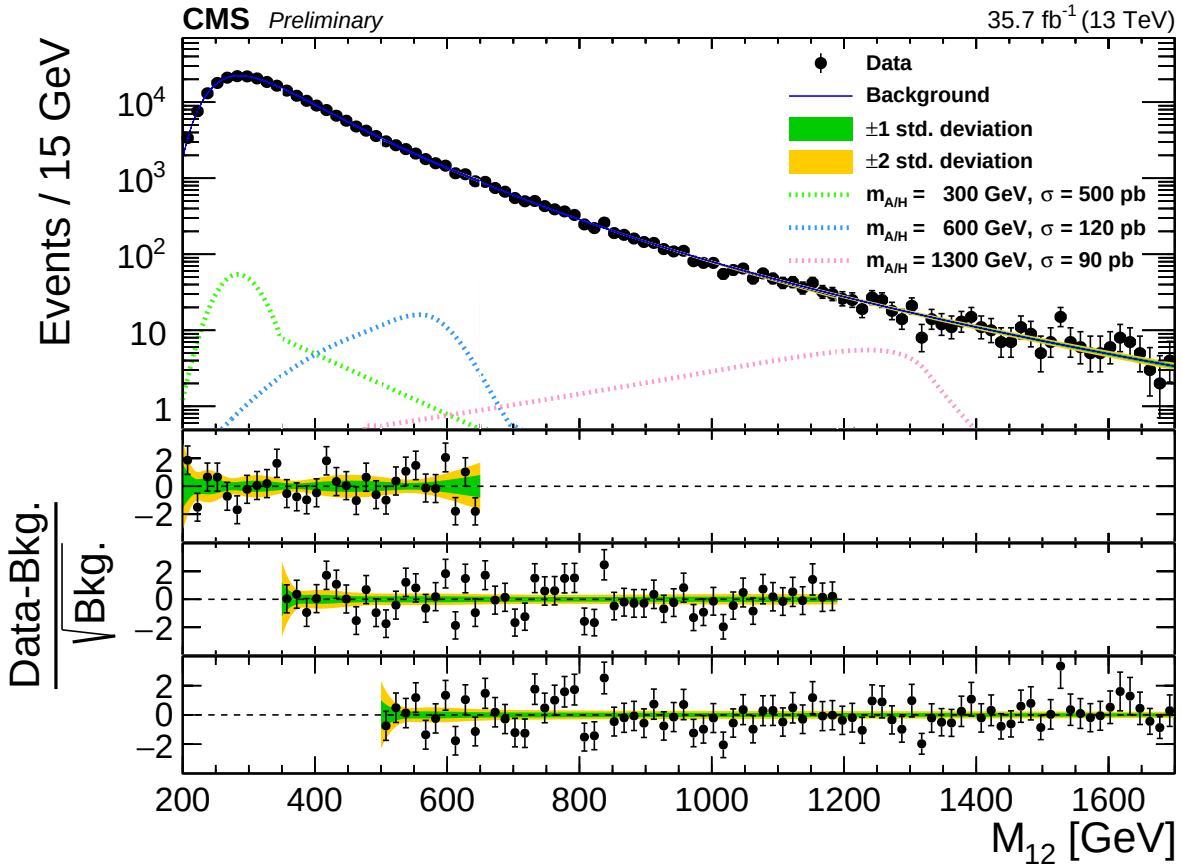

Figure 5: Distribution of the dijet mass M_{12} in the data triple-b-tag sample showing the three subranges together with the background-only fit. The shaded area shows the post-fit uncertainty. For illustration, the expected signal contribution for three representative mass points is shown, scaled to cross sections suitable for visualization. The kink at around 350 GeV of the 300 GeV signal shape is caused by the wrong-pairing background. In the bottom panels the normalized difference $(\frac{\text{Data}-\text{Bkg}}{\sqrt{\text{Bkg}}})$, where Bkg is the background as estimated by the fit, for the three subranges is shown.

of the mass of the Higgs boson in Fig. 6, extending the search range up to mass of 1300 GeV. The limits range from about 20 pb at 300 GeV, to about 0.4 pb at 1100 GeV. The limits are also summarized in Table 2 in the appendix.

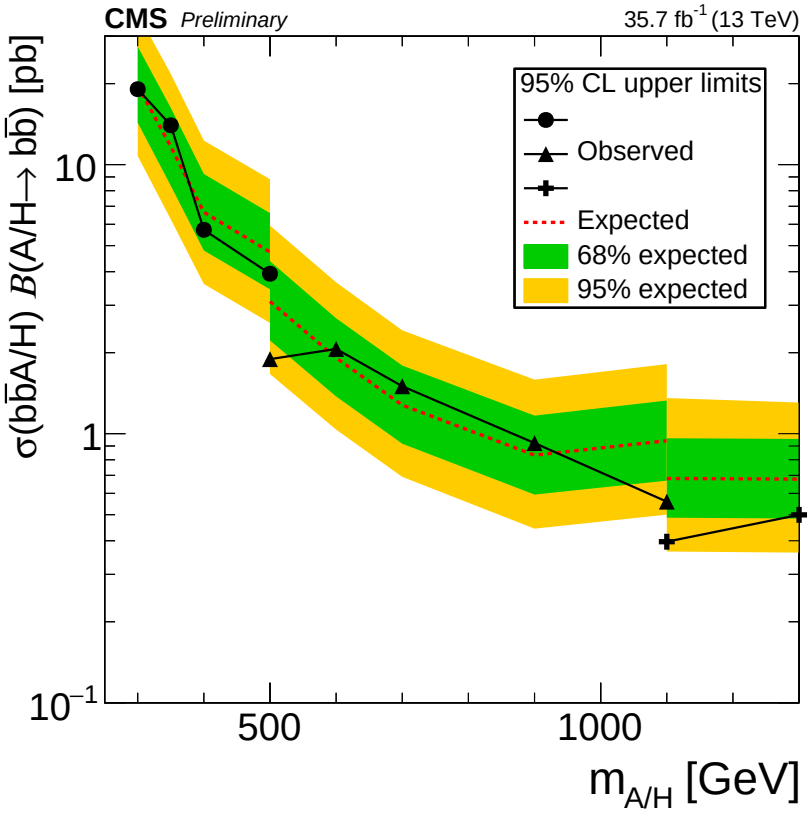

Figure 6: Expected and observed upper limits on $\sigma(\mathrm{pp} \to \mathrm{bA/H} + \mathrm{X})\,\mathcal{B}(\mathrm{A/H} \to \mathrm{b\bar{b}})$ at 95% CL as a function of the Higgs boson mass $m_{\mathrm{A/H}}$. For the observed limit, three different marker types are used to distinguish the three subranges in which the results have been obtained. The inner (green) band and the outer (yellow) band indicate the regions containing 68 and 95%, respectively, of the distribution of limits expected under the background-only hypothesis.

8.1 Interpretation within the MSSM

The cross section limits shown in Fig. 6 are translated into exclusion limits on the MSSM parameters $\tan\beta$ and m_{A}. The cross sections for $\mathrm{b} + \mathrm{H/A}$ associated production as obtained with the four-flavour NLO [59, 60] and the five-flavour NNLO QCD calculations implemented in BBH@NNLO [61] were combined using the Santander matching scheme [62]. The branching fractions were computed with the FEYNHIGGS [63–66] and HDECAY [67, 68] programs as described in Ref. [15].

The observed and expected 95% CL median upper limits on $\tan\beta$ versus m_{A} are shown in Fig. 7. They were computed within the MSSM $m_{\mathrm{h}}^{\mathrm{mod+}}$ benchmark scenario [7] with the higgsino mass parameter $\mu = +200$ GeV and in the hMSSM scenario [11–13]. In the former scenario, the observed upper limits range from $\tan\beta$ about 25 in the low-m_{A} region to about 60 at $m_{\mathrm{A}} = 750$ GeV. They considerably extend the preceding measurements at $\sqrt{s} = 7$ and 8 TeV [29, 30]. The model interpretation is not extended beyond masses 800 GeV, because the theoretical predictions are not reliable for $\tan\beta$ much higher than 60. Additional model interpretations for m_{A} vs. $\tan\beta$ in the light $\widetilde{\tau}$ and the light $\widetilde{\mathrm{t}}$ benchmark scenarios are given in Fig. 8, and in Tables 3–6 in the appendix.

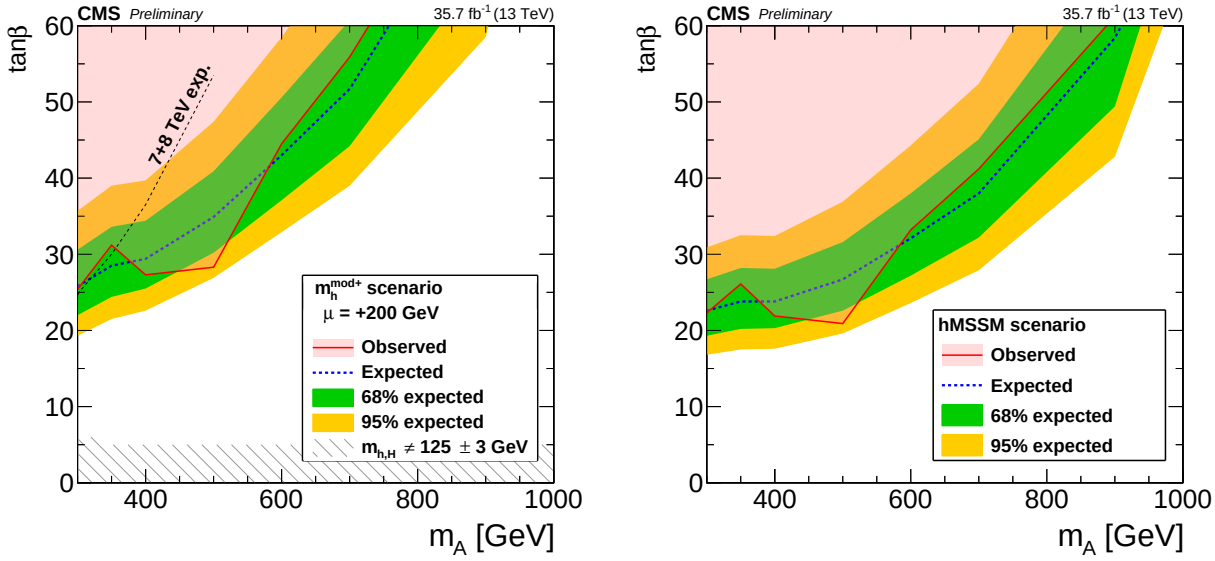

Figure 7: Expected and observed upper limits at 95% CL for $m_{\mathrm{A/H}}$ vs. the MSSM parameter $\tan\beta$ in the (left) $m_{\mathrm{h}}^{\mathrm{mod+}}$ benchmark scenario with $\mu = +200\,\mathrm{GeV}$, and (right) in the hMSSM scenario. The inner (green) band and the outer (yellow) band indicate the regions containing 68 and 95%, respectively, of the distribution of limits expected under the background-only hypothesis. The excluded parameter space is indicated by the red shaded area.

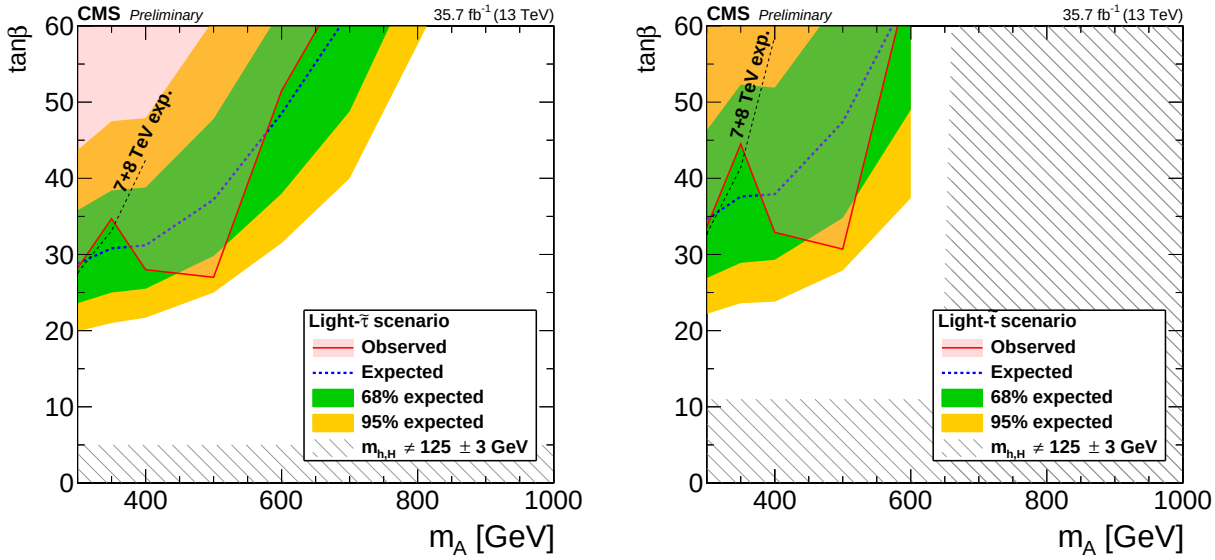

Figure 8: Expected and observed upper limits at 95% CL for $m_{\mathrm{A/H}}$ vs. the MSSM parameter $\tan\beta$ in the (left) light $\tilde{\tau}$ and the (right) light $\tilde{\mathrm{t}}$ benchmark scenarios. The inner (green) band and the outer (yellow) band indicate the regions containing 68 and 95%, respectively, of the distribution of limits expected under the background-only hypothesis. The excluded parameter space is indicated by the red shaded area.

8.2 Interpretation within the 2HDM

Cross sections and branching fractions for the bbH and bbA processes within different 2HDM models have been computed at NNLO using the SUSHI [69], 2HDMC [70] and LHAPDF [71] frameworks. The 2HDM parameters have been set according to the "Scenario G" proposed in Ref. [72]. Specifically, degeneracy of the heavier Higgs bosons is assumed ($m_A = m_H = m_{H^\pm}$) and the mixing term has been set to $m_{12}^2 = \frac{1}{2} m_A^2 \sin 2\beta$. The choice of such a MSSM-like parameterization allows using the same signal samples as for the MSSM analysis.

The results for the type-II and flipped models are displayed in Fig. 9 as upper limits for $\tan\beta$ as a function of $\cos(\beta - \alpha)$. Upper limits derived from the ATLAS $A \to Zh$ analysis [32] at a centre-of-mass energy of 13 TeV are shown as well. The results for the flipped model presented here provide the only experimental upper limits in the central region in $\cos(\beta - \alpha)$ and strong unique constraints on $\tan\beta$. Figure 10 shows the upper limits for $\tan\beta$ as a function of $\cos(\beta - \alpha)$ in the type-II and flipped models for $m_{A/H} = 500$ GeV.

9 Summary

A search for a heavy Higgs boson decaying into a b quark-antiquark pair and accompanied by at least one additional b quark has been performed. The data analyzed correspond to an integrated luminosity of 35.7 fb^{-1}, recorded in pp collisions at a centre-of-mass energy of 13 TeV at the LHC. For this purpose, dedicated triggers using all-hadronic jet signatures combined with online b tagging were developed. The signal is characterized by events with at least three b-tagged jets. The search has been performed in the invariant mass spectrum of the two leading b-tagged jets.

No evidence for a signal is found. Upper limits on the Higgs boson cross section times branching fraction are obtained in the mass region 300–1300 GeV at 95% confidence level. They range from about 20 pb at the lower end of the mass range, to about 0.4 pb at 1100 GeV, and extend to considerably higher masses than those accessible to previous analyses performed.

The results are interpreted within various MSSM benchmark scenarios. They yield upper limits on the model parameter $\tan\beta$ as a function of the mass parameter m_A. The observed limit for $\tan\beta$ ranges down to about 25 at the lowest m_A value of 300 GeV in the $m_h^{\text{mod+}}$ scenario with a higgsino mass parameter of $\mu = +200$ GeV. The results are also interpreted in the 2HDM type-II and flipped scenarios. The limits obtained for the flipped scenario provide the only experimental upper limits in the region around zero of $\cos(\beta - \alpha)$, and strong unique constraints on $\tan\beta$.

References

[1] H. P. Nilles, "Supersymmetry, supergravity and particle physics", *Phys. Rept.* **110** (1984) 1, doi:10.1016/0370-1573(84)90008-5.

[2] G. C. Branco et al., "Theory and phenomenology of two-Higgs-doublet models", *Phys. Rep.* **516** (2012) 1, doi:10.1016/j.physrep.2012.02.002, arXiv:1106.0034.

[3] ATLAS Collaboration, "Observation of a new particle in the search for the Standard Model Higgs boson with the ATLAS detector at the LHC", *Phys. Lett. B* **716** (2012) 1, doi:10.1016/j.physletb.2012.08.020, arXiv:1207.7214.

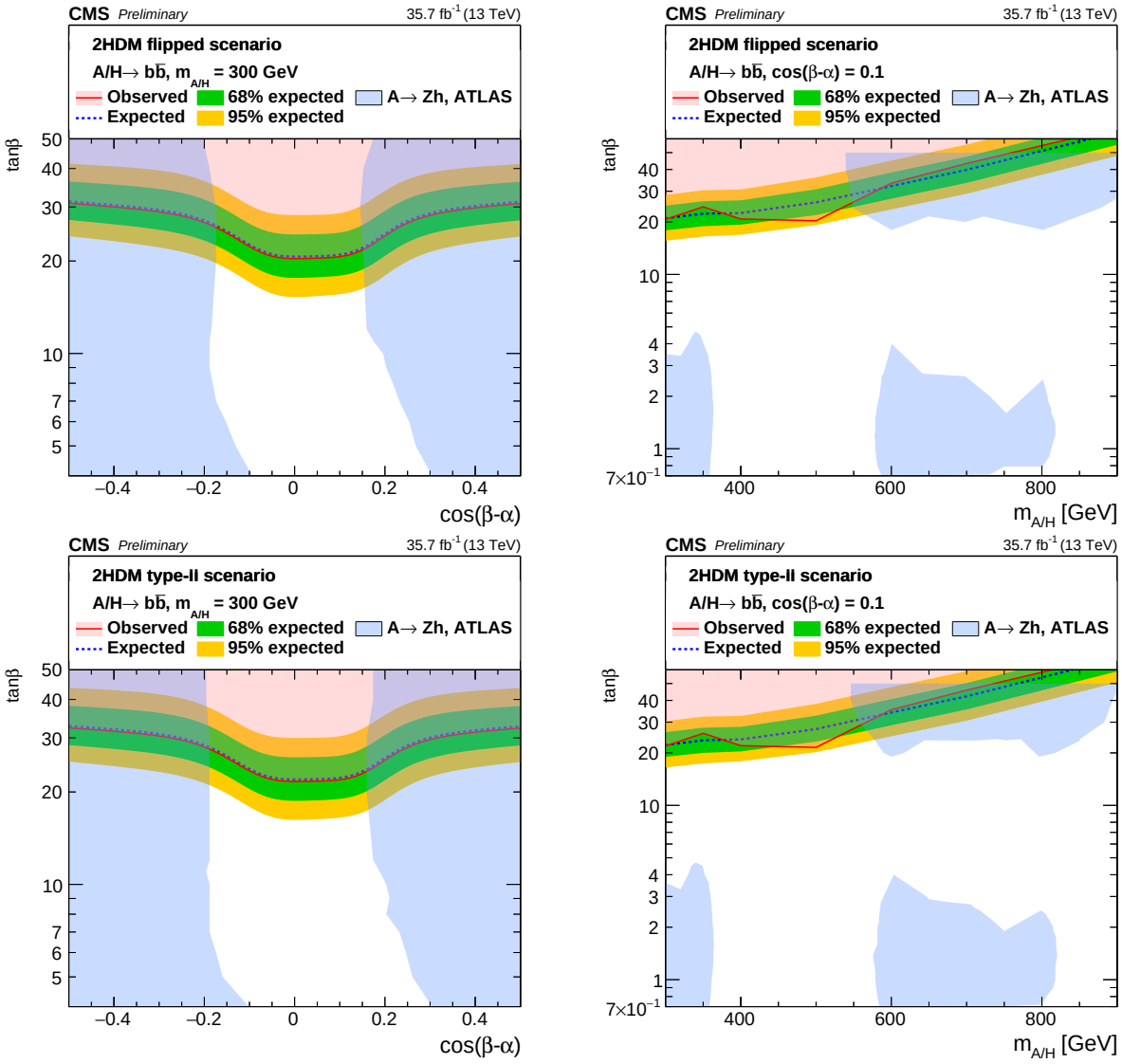

Figure 9: Upper limits for the parameter $\tan\beta$ at 95% confidence level for the flipped (upper) and type-II (lower) models, as a function of $\cos(\beta-\alpha)$ in the range of $[-0.5, 0.5]$ for the mass $m_{\mathrm{H}} = m_{\mathrm{A}} = 300$ GeV (left) and as a function of $m_{\mathrm{A/H}}$ when $\cos(\beta-\alpha) = 0.1$ (right). The results from the ATLAS A $\rightarrow$ Zh analysis [32] are also shown as blue shaded area for comparison which provide limits up to $\tan\beta$ of 50.

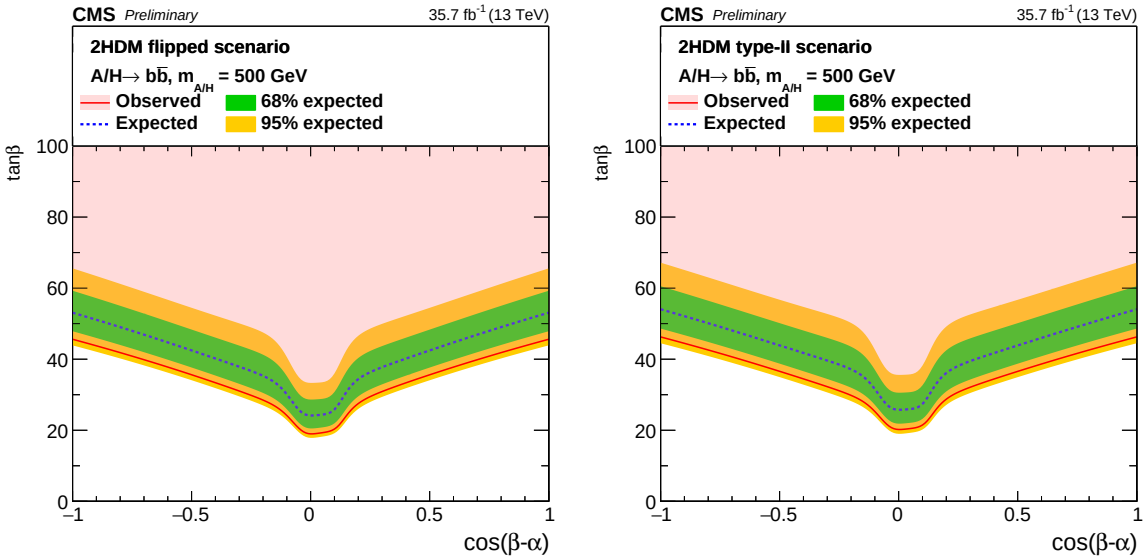

Figure 10: Upper limits for the parameter $\tan\beta$ at 95% confidence level for the flipped (left) and type-II (right) models as a function of $\cos(\beta-\alpha)$ in the full range of $[-1.0, 1.0]$, for the mass $m_{\mathrm{H}} = m_{\mathrm{A}} = 500$ GeV. The inner (green) band and the outer (yellow) band indicate the regions containing 68 and 95%, respectively, of the distribution of limits expected under the background-only hypothesis.

[4] CMS Collaboration, "Observation of a new boson at a mass of 125 GeV with the CMS experiment at the LHC", *Phys. Lett. B* **716** (2012) 30, doi:10.1016/j.physletb.2012.08.021, arXiv:1207.7235.

[5] CMS Collaboration, "Observation of a new boson with mass near 125 GeV in pp collisions at $\sqrt{s}$ = 7 and 8 TeV", *JHEP* **06** (2013) 081, doi:10.1007/JHEP06(2013)081, arXiv:1303.4571.

[6] M. Carena et al., "MSSM Higgs boson searches at the LHC: benchmark scenarios after the discovery of a Higgs-like particle", *Eur. Phys. J. C* **73** (2013) 2552, doi:10.1140/epjc/s10052-013-2552-1, arXiv:1302.7033.

[7] M. S. Carena, S. Heinemeyer, C. E. M. Wagner, and G. Weiglein, "MSSM Higgs boson searches at the Tevatron and the LHC: Impact of different benchmark scenarios", *Eur. Phys. J. C* **45** (2006) 797, doi:10.1140/epjc/s2005-02470-y, arXiv:hep-ph/0511023.

[8] ALEPH, DELPHI, L3, and OPAL Collaborations, LEP Working Group for Higgs Boson Searches, "Search for neutral MSSM Higgs bosons at LEP", *Eur. Phys. J. C* **47** (2006) 547, doi:10.1140/epjc/s2006-02569-7, arXiv:hep-ex/0602042.

[9] M. Carena, S. Heinemeyer, C. E. M. Wagner, and G. Weiglein, "Suggestions for benchmark scenarios for MSSM Higgs boson searches at hadron colliders", *Eur. Phys. J. C* **26** (2003) 601, doi:10.1140/epjc/s2002-01084-3, arXiv:hep-ph/0202167.

[10] S. Heinemeyer, W. Hollik, and G. Weiglein, "Constraints on $\tan\beta$ in the MSSM from the upper bound on the mass of the lightest Higgs boson", *JHEP* **06** (2000) 009, doi:10.1088/1126-6708/2000/06/009, arXiv:hep-ph/9909540.

[11] L. Maiani, A. D. Polosa, and V. Riquer, "Bounds to the Higgs Sector Masses in Minimal Supersymmetry from LHC Data", *Phys. Lett. B* **724** (2013) 274, doi:10.1016/j.physletb.2013.06.026, arXiv:1305.2172.

[12] A. Djouadi et al., "The post-Higgs MSSM scenario: Habemus MSSM?", *Eur. Phys. J. C* **73** (2013) 2650, doi:10.1140/epjc/s10052-013-2650-0, arXiv:1307.5205.

[13] A. Djouadi et al., "Fully covering the MSSM Higgs sector at the LHC", *JHEP* **06** (2015) 168, doi:10.1007/JHEP06(2015)168, arXiv:1502.05653.

[14] LHC Higgs Cross Section Working Group, "Benchmark scenarios for low tan β in the MSSM", Public Note LHCHXSWG-2015-002, CERN, Geneva, 2015.

[15] LHC Higgs Cross Section Working Group, "Handbook of LHC Higgs Cross Sections: 3. Higgs Properties", doi:10.5170/CERN-2013-004, arXiv:1307.1347.

[16] E. Izaguirre, G. Krnjaic, and B. Shuve, "Bottom-up approach to the Galactic Center excess", *Phys. Rev. D* **90** (2014) 055002, doi:10.1103/PhysRevD.90.055002, arXiv:1404.2018.

[17] A. Berlin, D. Hooper, and S. D. McDermott, "Simplified dark matter models for the Galactic Center gamma-ray excess", *Phys. Rev. D* **89** (2014) 115022, doi:10.1103/PhysRevD.89.115022, arXiv:1404.0022.

[18] CMS Collaboration, "Search for neutral Higgs bosons decaying to tau pairs in pp collisions at $\sqrt{s} = 7$ TeV", *Phys. Lett. B* **713** (2012) 68, doi:10.1016/j.physletb.2012.05.028, arXiv:1202.4083.

[19] ATLAS Collaboration, "Search for the neutral Higgs bosons of the minimal supersymmetric standard model in pp collisions at $\sqrt{s} = 7$ TeV with the ATLAS detector", *JHEP* **02** (2013) 095, doi:10.1007/JHEP02(2013)095, arXiv:1211.6956.

[20] CMS Collaboration, "Search for neutral MSSM Higgs bosons decaying to a pair of tau leptons in pp collisions", *JHEP* **10** (2014) 160, doi:10.1007/JHEP10(2014)160, arXiv:1408.3316.

[21] ATLAS Collaboration, "Search for neutral Higgs bosons of the minimal supersymmetric standard model in pp collisions at $\sqrt{s}$ = 8 TeV with the ATLAS detector", *JHEP* **11** (2014) 056, doi:10.1007/JHEP11(2014)056, arXiv:1409.6064.

[22] CMS Collaboration, "Search for a neutral MSSM Higgs boson decaying into $\tau\tau$ with 12.9 fb^{-1} of data at $\sqrt{s} = 13$ TeV", CMS Physics Analysis Summary CMS-PAS-HIG-16-037, CERN, Geneva, 2016.

[23] ATLAS Collaboration, "Search for additional heavy neutral Higgs and gauge bosons in the ditau final state produced in 36 fb^{-1} of pp collisions at $\sqrt{s} = 13$ TeV with the ATLAS detector", *JHEP* **01** (2018) 055, doi:10.1007/JHEP01(2018)055, arXiv:1709.07242.

[24] CDF Collaboration, "Search for Higgs Bosons Predicted in Two-Higgs-Doublet Models via Decays to Tau Lepton Pairs in 1.96 TeV $p\bar{p}$ Collisions", *Phys. Rev. Lett.* **103** (2009) 201801, doi:10.1103/PhysRevLett.103.201801, arXiv:0906.1014.

[25] D0 Collaboration, "Search for Higgs Bosons Decaying to Tau Pairs in $p\bar{p}$ Collisions with the D0 Detector", *Phys. Rev. Lett.* **101** (2008) 071804, doi:10.1103/PhysRevLett.101.071804, arXiv:0805.2491.

[26] D0 Collaboration, "Search for Higgs bosons of the minimal supersymmetric standard model $p\bar{p}$ in collisions at $\sqrt{s} = 1.96$ TeV", *Phys. Lett. B* **710** (2012) 569, doi:10.1016/j.physletb.2012.03.021, arXiv:1112.5431.

[27] CMS Collaboration, "Search for neutral MSSM Higgs bosons decaying to $\mu^+\mu^-$ in pp collisions at $\sqrt{s} = 7$ and 8 TeV", *Phys. Lett. B* **752** (2016) 221, doi:10.1016/j.physletb.2015.11.042, arXiv:1508.01437.

[28] CDF and D0 Collaborations, "Search for neutral Higgs bosons in events with multiple bottom quarks at the Tevatron", *Phys. Rev. D* **86** (2012) 091101, doi:10.1103/PhysRevD.86.091101, arXiv:1207.2757.

[29] CMS Collaboration, "Search for a Higgs boson decaying into a b-quark pair and produced in association with b quarks in proton-proton collisions at 7 TeV", *Phys. Lett. B* **722** (2013) 207, doi:10.1016/j.physletb.2013.04.017, arXiv:1302.2892.

[30] CMS Collaboration, "Search for neutral MSSM Higgs bosons decaying into a pair of bottom quarks", *JHEP* **11** (2015) 071, doi:10.1007/JHEP11(2015)071, arXiv:1506.08329.

[31] ATLAS Collaboration, "Search for a CP-odd Higgs boson decaying to Zh in pp collisions at $\sqrt{s} = 8$ TeV with the ATLAS detector", *Phys. Lett. B* **744** (2015) 163, doi:10.1016/j.physletb.2015.03.054, arXiv:1502.04478.

[32] ATLAS Collaboration, "Search for heavy resonances decaying into a W or Z boson and a Higgs boson in final states with leptons and b-jets in 36Zfb^{-1} of $\sqrt{s} = 13$ TeV pp collisions with the ATLAS detector", (2017). arXiv:1712.06518. Submitted to *JHEP*.

[33] CMS Collaboration, "The CMS experiment at the CERN LHC", *JINST* **3** (2008) S08004, doi:10.1088/1748-0221/3/08/S08004.

[34] CMS Collaboration, "Particle-flow reconstruction and global event description with the CMS detector", *JINST* **12** (2017) P10003, doi:10.1088/1748-0221/12/10/P10003, arXiv:1706.04965.

[35] CMS Collaboration, "Description and performance of track and primary-vertex reconstruction with the CMS tracker", *JINST* **9** (2014) P10009, doi:10.1088/1748-0221/9/10/P10009, arXiv:1405.6569.

[36] M. Cacciari, G. P. Salam, and G. Soyez, "The anti-k_t jet clustering algorithm", *JHEP* **04** (2008) 063, doi:10.1088/1126-6708/2008/04/063, arXiv:0802.1189.

[37] M. Cacciari, G. P. Salam, and G. Soyez, "FastJet User Manual", *Eur. Phys. J. C* **72** (2012) doi:10.1140/epjc/s10052-012-1896-2, arXiv:1111.6097.

[38] CMS Collaboration, "Pileup removal algorithms", CMS Physics Analysis Summary CMS-PAS-JME-14-001, CERN, 2014.

[39] M. Cacciari and G. P. Salam, "Pileup subtraction using jet areas", *Phys. Lett. B* **659** (2008) 119, doi:10.1016/j.physletb.2007.09.077, arXiv:0707.1378.

[40] CMS Collaboration, "Jet energy scale and resolution in the CMS experiment in pp collisions at 8 TeV", *JINST* **12** (2017) P02014, doi:10.1088/1748-0221/12/02/P02014, arXiv:1607.03663.

[41] CMS Collaboration, "Identification of heavy-flavour jets with the CMS detector in pp collisions at 13 TeV", (2017). arXiv:1712.07158. Submitted to *JINST*.

[42] T. Sjöstrand, S. Mrenna, and P. Skands, "A brief introduction to PYTHIA 8.1", *Comp. Phys. Comm.* **178** (2008) 852, doi:10.1016/j.cpc.2008.01.036, arXiv:0710.3820.

[43] LHC Higgs Cross Section Working Group, S. Dittmaier et al., "Handbook of LHC Higgs Cross Sections: 2. Differential Distributions", doi:10.5170/CERN-2012-002, arXiv:1201.3084.

[44] J. Alwall et al., "The automated computation of tree-level and next-to-leading order differential cross sections, and their matching to parton shower simulations", *JHEP* **07** (2014) 079, doi:10.1007/JHEP07(2014)079, arXiv:1405.0301.

[45] M. Wiesemann et al., "Higgs production in association with bottom quarks", *JHEP* **02** (2015) 132, doi:10.1007/JHEP02(2015)132, arXiv:1409.5301.

[46] R. Frederix, S. Frixione, F. Maltoni, and T. Stelzer, "Automation of next-to-leading order computations in QCD: The FKS subtraction", *JHEP* **10** (2009) 003, doi:10.1088/1126-6708/2009/10/003, arXiv:0908.4272.

[47] V. Hirschi et al., "Automation of one-loop QCD corrections", *JHEP* **05** (2011) 044, doi:10.1007/JHEP05(2011)044, arXiv:1103.0621.

[48] R. D. Ball et al., "Impact of Heavy Quark Masses on Parton Distributions and LHC Phenomenology", *Nucl. Phys. B* **849** (2011) 296, doi:10.1016/j.nuclphysb.2011.03.021, arXiv:1101.1300.

[49] CMS Collaboration, "Event generator tunes obtained from underlying event and multiparton scattering measurements", *Eur. Phys. J. C* **76** (2016) 155, doi:10.1140/epjc/s10052-016-3988-x, arXiv:1512.00815.

[50] GEANT4 Collaboration, "GEANT4: a simulation toolkit", *Nucl. Instrum. Meth. A* **506** (2003) 250, doi:10.1016/S0168-9002(03)01368-8.

[51] CMS Collaboration, "The CMS trigger system", *JINST* **12** (2017) P01020, doi:10.1088/1748-0221/12/01/P01020, arXiv:1609.02366.

[52] Belle Collaboration, "A detailed test of the CsI(Tl) calorimeter for BELLE with photon beams of energy between 20-MeV and 5.4-GeV", *Nucl. Instrum. Meth. A* **441** (2000) 401, doi:10.1016/S0168-9002(99)00992-4.

[53] CMS Collaboration, "Search for massive resonances decaying into WW, WZ or ZZ bosons in proton-proton collisions at $\sqrt{s} = 13$ TeV", *JHEP* **03** (2017) 162, doi:10.1007/JHEP03(2017)162, arXiv:1612.09159.

[54] CMS Collaboration, "CMS Luminosity Measurements for the 2016 Data Taking Period", CMS Physics Analysis Summary CMS-PAS-LUM-17-001, CERN, Geneva, 2017.

[55] LHC Higgs Cross Section Working Group, D. de Florian et al., "Handbook of LHC Higgs Cross Sections: 4. Deciphering the Nature of the Higgs Sector", doi:10.23731/CYRM-2017-002, arXiv:1610.07922.

[56] T. Junk, "Confidence level computation for combining searches with small statistics", *Nucl. Instrum. Meth. A* **434** (1999) 435, doi:10.1016/S0168-9002(99)00498-2, arXiv:hep-ex/9902006.

[57] A. L. Read, "Presentation of search results: The CL_s technique", *J. Phys. G* **28** (2002) 2693, doi:10.1088/0954-3899/28/10/313.

[58] L. Moneta et al., "The RooStats Project", in *13th International Workshop on Advanced Computing and Analysis Techniques in Physics Research (ACAT2010)*. SISSA, 2010. arXiv:1009.1003.

[59] S. Dittmaier, M. Krämer, and M. Spira, "Higgs radiation off bottom quarks at the Tevatron and the CERN LHC", *Phys. Rev. D* **70** (2004) 074010, doi:10.1103/PhysRevD.70.074010, arXiv:hep-ph/0309204.

[60] S. Dawson, C. B. Jackson, L. Reina, and D. Wackeroth, "Exclusive Higgs boson production with bottom quarks at hadron colliders", *Phys. Rev. D* **69** (2004) 074027, doi:10.1103/PhysRevD.69.074027, arXiv:hep-ph/0311067.

[61] R. V. Harlander and W. B. Kilgore, "Higgs boson production in bottom quark fusion at next-to-next-to leading order", *Phys. Rev. D* **68** (2003) 013001, doi:10.1103/PhysRevD.68.013001, arXiv:hep-ph/0304035.

[62] R. V. Harlander, M. Krämer, and M. Schumacher, "Bottom-quark associated Higgs-boson production: reconciling the four- and five-flavour scheme approach", CERN Preprint, 2011. arXiv:1112.3478.

[63] G. Degrassi et al., "Towards high-precision predictions for the MSSM Higgs sector", *Eur. Phys. J. C* **28** (2003) 133, doi:10.1140/epjc/s2003-01152-2, arXiv:hep-ph/0212020.

[64] M. Frank et al., "The Higgs boson masses and mixings of the complex MSSM in the Feynman-diagrammatic approach", *JHEP* **02** (2007) 047, doi:10.1088/1126-6708/2007/02/047, arXiv:hep-ph/0611326.

[65] S. Heinemeyer, W. Hollik, and G. Weiglein, "FeynHiggs: A program for the calculation of the masses of the neutral CP even Higgs bosons in the MSSM", *Comput. Phys. Commun.* **124** (2000) 76, doi:10.1016/S0010-4655(99)00364-1, arXiv:hep-ph/9812320.

[66] S. Heinemeyer, W. Hollik, and G. Weiglein, "The Masses of the neutral CP - even Higgs bosons in the MSSM: Accurate analysis at the two loop level", *Eur. Phys. J. C* **9** (1999) 343, doi:10.1007/s100529900006, arXiv:hep-ph/9812472.

[67] A. Djouadi, J. Kalinowski, and M. Spira, "HDECAY: A Program for Higgs boson decays in the standard model and its supersymmetric extension", *Comput. Phys. Commun.* **108** (1998) 56, doi:10.1016/S0010-4655(97)00123-9, arXiv:hep-ph/9704448.

[68] A. Djouadi, M. M. Mühlleitner, and M. Spira, "Decays of supersymmetric particles: The Program SUSY-HIT", in *Physics at LHC. Proceedings, 3rd Conference, Cracow, Poland, July 3-8, 2006*, volume 38, p. 635. 2007. arXiv:hep-ph/0609292.

[69] R. V. Harlander, S. Liebler, and H. Mantler, "SusHi: A program for the calculation of Higgs production in gluon fusion and bottom-quark annihilation in the Standard Model and the MSSM", *Comput. Phys. Commun.* **184** (2013) 1605, doi:10.1016/j.cpc.2013.02.006, arXiv:1212.3249.

[70] D. Eriksson, J. Rathsman, and O. Stål, "2HDMC: Two-Higgs-Doublet Model Calculator Physics and Manual", *Comput. Phys. Commun.* **181** (2010) 189, doi:10.1016/j.cpc.2009.09.011, arXiv:0902.0851.

[71] A. Buckley et al., "LHAPDF6: parton density access in the LHC precision era", *Eur. Phys. J. C* **75** (2015) 132, doi:10.1140/epjc/s10052-015-3318-8, arXiv:1412.7420.

[72] H. E. Haber and O. Stål, "New LHC benchmarks for the $\mathcal{CP}$ -conserving two-Higgs-doublet model", *Eur. Phys. J. C* **75** (2015) 491, doi:10.1140/epjc/s10052-015-3697-x, arXiv:1507.04281. [Erratum: *Eur. Phys. J. C* **76**,312(2016)].

Appendix A Signal Efficiency

The signal efficiency as a function of the Higgs boson mass is summarized in Table 1.

Table 1: The total signal efficiency in per mille as a function of the Higgs boson mass $m_{\mathrm{A/H}}$.

$m_{\mathrm{A/H}}$ [GeV]	Efficiency [per mille]
300	7.23
350	10.5
400	12.6
500	14.0
600	13.6
700	12.5
900	9.41
1100	6.87
1300	4.89

Appendix B Exclusion limits

The model-independent $\mathrm{CL_s}$ limits on $\sigma(\mathrm{pp} \to \mathrm{bA/H} + \mathrm{X})\,\mathcal{B}(\mathrm{A/H} \to \mathrm{b\bar{b}})$ are listed in Table 2 for different Higgs boson masses $m_{\mathrm{A/H}}$. The $\mathrm{CL_s}$ limits of $(\tan\beta, m_{\mathrm{A}})$ are listed in Tables 3 to 6 for different MSSM benchmark scenarios with $\mu = +200\,\mathrm{GeV}$.

Table 2: Expected and observed $\mathrm{CL_s}$ upper limits on $\sigma(\mathrm{pp} \to \mathrm{bA/H} + \mathrm{X})\,\mathcal{B}(\mathrm{A/H} \to \mathrm{b\bar{b}})$ in pb as a function of $m_{\mathrm{A/H}}$, as obtained from the 13 TeV data.

Mass [GeV]	-2σ	-1σ	Median	$+1\sigma$	$+2\sigma$	Observed
300	10.8	14.3	19.7	27.5	36.5	19.1
350	6.3	8.4	11.7	16.3	21.7	14.0
400	3.6	4.8	6.7	9.2	12.3	5.7
500	1.7	2.2	3.1	4.4	5.9	1.9
600	1.0	1.4	1.9	2.7	3.7	2.1
700	0.7	0.9	1.3	1.8	2.4	1.5
900	0.4	0.6	0.8	1.2	1.6	0.9
1100	0.36	0.49	0.68	0.96	1.36	0.40
1300	0.36	0.48	0.68	0.96	1.31	0.50

Table 3: Expected and observed CL_s upper limits on $\tan\beta$ as a function of m_A in the m_h^{mod+}, $\mu = +200\,GeV$, benchmark scenario obtained from a 13 TeV data. Since theoretical predictions for $\tan\beta > 60$ are not reliable, cells for which $\tan\beta$ would exceed this value are indicated by —.

Mass [GeV]	-2σ	-1σ	Median	$+1\sigma$	$+2\sigma$	Observed
300	19.3	22.0	25.8	30.6	35.7	25.4
350	21.5	24.4	28.5	33.6	39.0	31.2
400	22.6	25.5	29.4	34.4	39.7	27.3
500	26.9	30.2	34.9	40.9	47.4	28.3
600	32.9	37.1	43.0	50.6	58.5	44.5
700	39.0	44.2	51.7	—	—	55.9
900	58.5	—	—	—	—	—

Table 4: Expected and observed CL_s upper limits on $\tan\beta$ as a function of m_A in the hMSSM, $\mu = +200\,GeV$, benchmark scenario obtained from a 13 TeV data. Since theoretical predictions for $\tan\beta > 60$ are not reliable, cells for which $\tan\beta$ would exceed this value are indicated by —.

Mass [GeV]	-2σ	-1σ	Median	$+1\sigma$	$+2\sigma$	Observed
300	16.8	19.3	22.6	26.7	30.9	22.3
350	17.5	20.2	23.8	28.2	32.5	26.1
400	17.6	20.3	23.8	28.1	32.4	21.9
500	19.6	22.6	26.7	31.6	36.9	20.9
600	23.6	27.2	32.1	38.0	44.3	33.2
700	27.9	32.2	38.0	45.1	52.4	41.2
900	42.8	49.4	58.4	—	—	—

Table 5: Expected and observed CL_s upper limits on $\tan\beta$ as a function of m_A in the light $\widetilde{\tau}$, $\mu = +200\,GeV$, benchmark scenario. Since theoretical predictions for $\tan\beta > 60$ are not reliable, cells for which $\tan\beta$ would exceed this value are indicated by —.

Mass [GeV]	-2σ	-1σ	Median	$+1\sigma$	$+2\sigma$	Observed
300	19.9	23.6	28.8	35.8	43.7	28.2
350	21.0	25.0	30.8	38.4	47.5	34.7
400	21.7	25.5	31.2	38.8	47.9	28.0
500	25.0	29.8	37.2	47.8	—	27.0
600	31.5	38.0	48.5	—	—	51.5
700	40.0	48.8	—	—	—	—

Table 6: Expected and observed CL_s upper limits on $\tan\beta$ as a function of m_A in the light $\tilde{t}$, $\mu = +200\,\text{GeV}$, benchmark scenario. Since theoretical predictions for $\tan\beta > 60$ are not reliable, cells for which $\tan\beta$ would exceed this value are indicated by —.

Mass [GeV]	-2σ	-1σ	Median	$+1\sigma$	$+2\sigma$	Observed
300	22.2	26.9	34.6	46.3	—	33.6
350	23.6	28.9	37.6	52.3	—	44.5
400	23.8	29.3	37.9	51.9	—	32.9
500	27.9	34.8	47.4	—	—	30.7
600	37.4	49.0	—	—	—	—